Multi-Angular Electroretinography (maERG): Topographic mapping of the retinal function combining real and virtual electrodes

Mercedes Gauthier*, Antoine Brassard-Simard, Mathieu Gauvin, Pierre Lachapelle†, and Jean-Marc Lina†

***Abstract*— *Goal:* The full-field electroretinogram (ffERG) is an objective tool to assess global retinal function, though as it is currently done, it is unable to localize sources of retinal dysfunction or damage. To overcome this, we have developed a new way to record multiple spatial derivations of the ERG using the rotating capability of the eye, thus creating "virtual electrodes". We have termed this the multi-angular ERG (or maERG). With only 3 real electrodes and 11 varying gaze positions, we create 33 "virtual electrodes". *Methods:* We created a realistic electrophysiological and anatomical eye model (i.e. forward model) to reconstruct the retinal activity (i.e. inverse problem) from the 33 virtual electrodes. We simulated 2 pathological scenarios (central and peripheral scotomas), which were compared to their respective theoretical source configurations using an Area under Receiver Operator Characteristic curve metric. *Results:* Our simulations show that the low-resolution brain electromagnetic tomography algorithm (LORETA) is the best method tested to reconstruct retinal sources when compared to the Minimum Norm Estimate algorithm. Furthermore, a signal to noise ratio of 50dB is needed to accurately reconstruct the retina's functional map. *Conclusion:* Our proposed maERG recording method, combined with our solution to the electromagnetic inverse problem enables us to reconstruct the functional map of the human retina. *Significance:* We believe that this new functional retinal imaging technique will permit earlier detection of retinal malfunction and consequently optimize the clinical monitoring of patients affected with retinopathies.**

***Index Terms*— Electroretinogram, inverse problem, multi-electrode, retina, virtual electrodes, wavelet transform.**

I. Introduction

In order to objectively assess retinal function, ophthalmologists rely on the full-field electroretinogram (ffERG), which is the electrical potential produced by the retina when stimulated by a flash of light. This signal is usually recorded with a single active electrode placed on the cornea or near it while reference and ground electrodes are placed at the external canthus and forehead, respectively [1]. Diagnoses of retinal diseases are generally obtained by comparing the peak time and amplitude of specific components of the ERG (such as the a- and b-waves) with reference data. An impaired a-wave is indicative of an anomaly of the outer retina (rod and cone photoreceptors), while an abnormal b-wave points to a defect in the inner retina (bipolar cells to ganglion cells). However, given that the stimulus normally used is diffuse light, the entire retina participates to the genesis of this response. This, combined with the fact that a single active electrode (usually placed on the cornea) is used for the recording, makes it impossible to localize where, on the retina, the pathological loci are. For example, small scotomas (i.e. patches of nonfunctional retina, surrounded by functional retina) cannot be detected with the ffERG. However, they can be detected by changing the flash stimulus to a specific pattern stimulus, as is done with the multifocal ERG (mfERG), which is also recorded using the same electrode montage as above [2].

The mfERG stimulus consists of an array of hexagons (usually 61 or 103) that covers approximately 50° of visual angle centered at the fovea (center of the macula) [3]. Each hexagon is illuminated with a mutually orthogonal sequence so that the response from each hexagon can be obtained, yielding a map of retinal function around the macula. Unfortunately, this technique only provides measurements of the central 40°–50° of the visual field [4], hence ignoring the peripheral retina. However, the latter region may contain vital clues about the progression of certain retinopathies, such as retinitis pigmentosa, a degenerative disease affecting 1/5000 to 1/3000 people worldwide [5].

To allow for the localization of small abnormal retinal sources at any given position on the retina, Davey *et al.* [6] have considered combining the diffuse ffERG stimulus with multiple recording electrodes to generate multiple simultaneously recorded ERGs (i.e., as many as there are recording electrodes). By solving the inverse field theory equations (i.e., computing

This work was supported by grants-in aid from the Canadian Institutes for Health Research (CIHR; MOP-126082), as well as the Richard Brotto-Zorina Ali and family studentship Award.

*M. Gauthier and A. Brassard-Simard are with the École de Technologie Supérieure and the McGill University Health Centre/Montreal Children's Hospital, Montreal, Quebec, Canada. (correspondence e-mail: mercedes.gauthier@mail.mcgill.ca).

M. Gauvin and P. Lachapelle are with the McGill University Health Centre/Montreal Children's Hospital, Montreal, Quebec, Canada.

J.-M. Lina is with the École de Technologie Supérieure and the Centre de Recherches Mathématiques, Montreal, Quebec, Canada.

†Equal last authors.

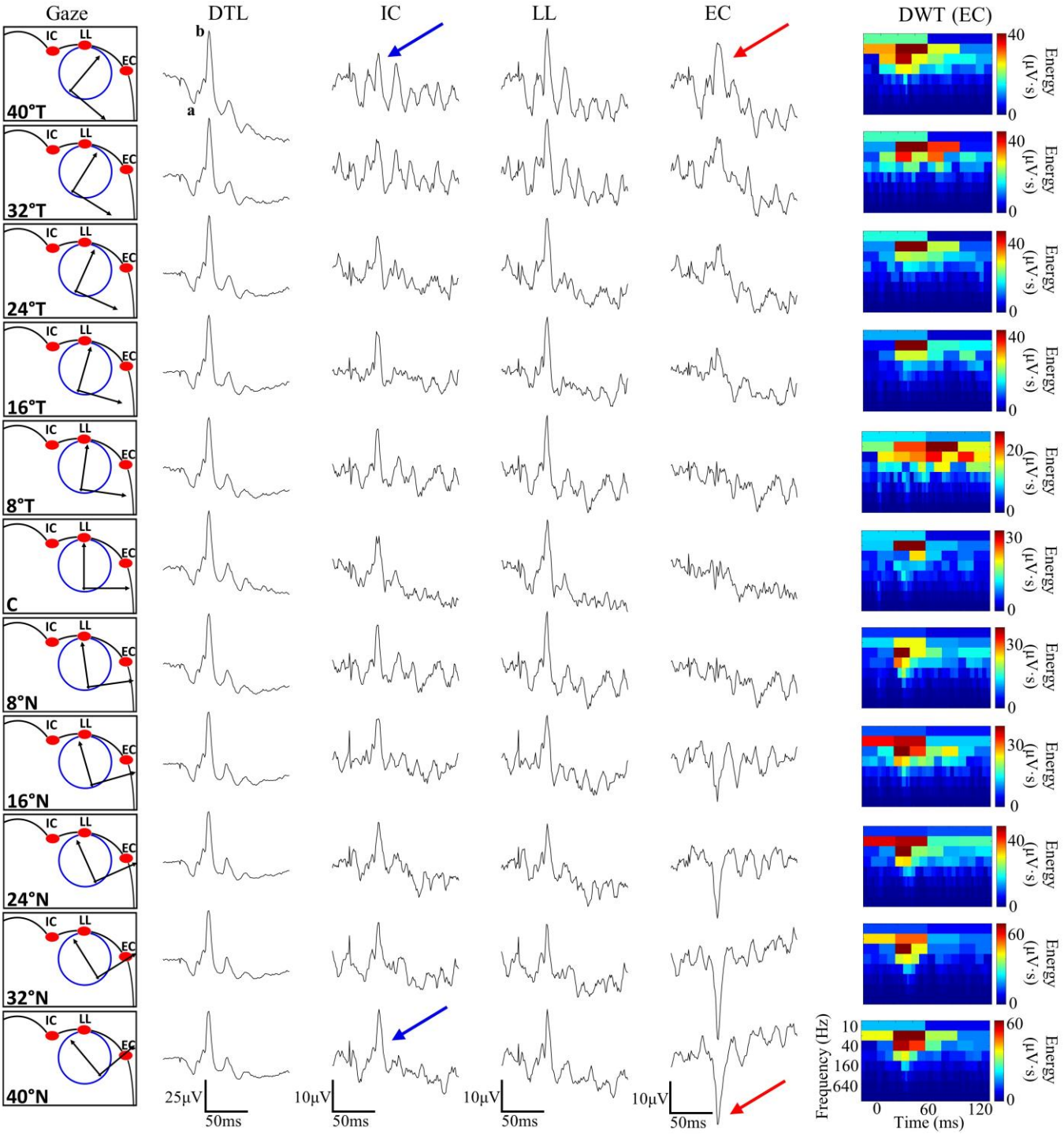

Fig. 1. ERG recordings from the different gaze positions (1st column; schematic view from the top of eye position in head), recorded with a DTL electrode (2nd column), the internal canthus electrode (IC; 3rd column), the lower lid electrode (LL; 4th column) and the external canthus electrode (EC; 5th column). The last column shows the DWT scalograms of the external canthus electrode recordings. Blue arrows show how the IC signals lose their a- and b-waves, when moving the gaze from nasal to temporal. Red arrows show how the EC signal starts positive at 40°T and slowly inverts and becomes negative at 40°N. A- and b-waves are identified on the ERG shown on the top left corner.

the retinal currents from measured electric voltages), the light-evoked electrical activity distribution would then be determined throughout the entire retina. Davey *et al.* [6] were able to analytically approximate the retinotopic distribution of retinal activity using 6 active needle electrodes placed on a bullfrog's eye, which yielded a retinal map of 6 functional regions. Consequently, a much larger number of electrodes would be required in order to generate the spatial resolution required for a reasonable diagnostic power. For comparison, electro-encephalograms (EEGs) recorded with the goal of reconstructing the cortical source distribution typically requires >32 electrodes to achieve optimal spatial resolution [7].

With the present work, we propose a solution that virtually increases the number of electrodes thus allowing a better spatial

resolution of the reconstructions. The principle is to combine three (real) electrodes placed around the eye with 11 different gaze positions to generate 33 "virtual electrodes" that will be used to record multiple, quasi-simultaneous responses, an approach that we termed the *multi-angular* ERG (or maERG).

Assuming that the different gaze positions do yield complementary information on the light-evoked retinal response, our goal is to use the maERG recordings to reconstruct (or project back on the retina) the retinal activity that generated these signals. This is achieved using the same methodology as that currently employed in the field of brain imaging, where multiple derivations (each recorded with a different electrode) of the EEG are used to solve the inverse problem, thus providing us with a topographical map of the underlying brain activity [8]. In order to validate if a similar approach could be used with the maERG, we first created a forward model of the eye and its theoretical retinal activity, and then solved the inverse problem with the use of simulated ERG signals.

Our main hypothesis is that the 33 maERG responses, combined with a human anatomical eye model, will yield a valid reconstruction that will enable us to topographically map the underlying retinal activity. To that end, the aim of this paper is first to introduce our new maERG recording procedure, and second to describe a reconstruction algorithm of the retinal activity based on the maERG recordings. To do so, we first solved the forward problem. It amounts to defining a source space (retina) and a realistic anatomical eye model to project the retina activity onto the cornea. From this generative setup able to define a forward model, we then solved an inverse problem to map the ERG measurements back onto the retina. The maERG protocol and the related source localization algorithm are the main topics of the present work.

II. The maERG Acquisition: Principles and Examples

A. The maERG Recording Principle and Procedure

The recording protocol used was previously approved by the Institutional Review Board of the Montreal Children's Hospital and was in accordance with the Declaration of Helsinki. Photopic maERG recordings (Diagnosys Espion system [Diagnosys LLC, Lowell, MA]; sampling frequency: 3413.33Hz; bandwidth: 1.25–1000Hz; flash intensities: 5 cd·s.m^{-2}; background: 30 cd.m^{-2}; averages between 20 and 30 flashes per response) were obtained from 6 normal voluntary subjects (4 females, 2 males; average age: 26.5±4.0 years). Subjects' heads were positioned on a chin rest placed in front of a Ganzfeld stimulator (ColorDome full-field stimulator; Diagnosys LLC, Lowell, MA), whose shape and diffuse light enables uniform illumination on the retina. Three active skin electrodes (Grass gold cup electrodes filled with Grass EC2 conductive cream) were placed close to the right eye (lower lid (LL) centered with the pupil, external canthus (EC) and internal canthus (IC); reference above the eyebrow, ground on forehead). Combining these 3 electrodes with the 11 gaze positions (40°, 32°, 24°, 16°, 8° temporal, central, 8°, 16°, 24°, 32°, 40° nasal; fixation was monitored and validated with an incorporated camera in the Ganzfeld) yielded a total of 33 (11x3) virtual electrodes and consequently 33 spatially distinct ERG waveforms. These were combined to another 11 virtual electrodes from the DTL control data (XStatic® conductive yarn, Sauquoit Industries, Scranton, PA, USA), placed in the inferior conjunctival bag of the right eye [9]. The resulting ERG signals were subsequently imported and analyzed in Matlab R2019a (MathWorks, Natick, MA, USA). The b-wave amplitude differences were quantified using the coefficient of variation (CV) which is a % ratio obtained by dividing the standard deviation by the mean (x100). This ratio was calculated from all ERG b-waves recorded (i.e., for each gaze direction and for each electrode position).

B. Examples of maERG Recordings in Healthy Subjects

In order for the maERG to yield useful information, the recordings must vary with the electrode and gaze positions, but not between the different trials. Fig. 1 shows maERG recordings from a representative subject. The latter are compared to maERGs recorded with the DTL electrode whose ERGs are not expected to yield positional waveform differences given that they make contact with the eye throughout its length. This claim is confirmed with the near-identical morphologies of all the DTL ERG waveforms shown in Fig. 1 (DTL column). Comparing the amplitudes of ERGs recorded at the most extreme temporal and nasal positions [i.e., 40o; normalized to the central gaze position (normal position for the recording of clinical ERGs) to minimize intersubject variability] reveals that they are not significantly different from each other (0.93±0.11 vs 0.85±0.04; p=0.198). In contrast, noticeable differences of ERG waveforms are observed in the recordings obtained with the IC and EC electrodes and to a lesser extent with the LL electrode, where gaze positions appear to significantly impact the morphology of the resulting ERG signal.

For example, the ERG signals recorded with the IC electrode include well-defined negative (i.e. a-wave) and positive (i.e. b-wave) waves at the 40° nasal position (bottom tracing of Fig. 1, IC column, seen in all 6 subjects), which are gradually replaced by a more oscillatory signal with progressive displacement of the direction of gaze towards more temporal positions (compare signals with blue arrows in Fig. 1, seen in 4/6 subjects; the other 2 subjects had less oscillatory, more b-wave type signals at the start). In comparison, responses recorded with the EC electrode

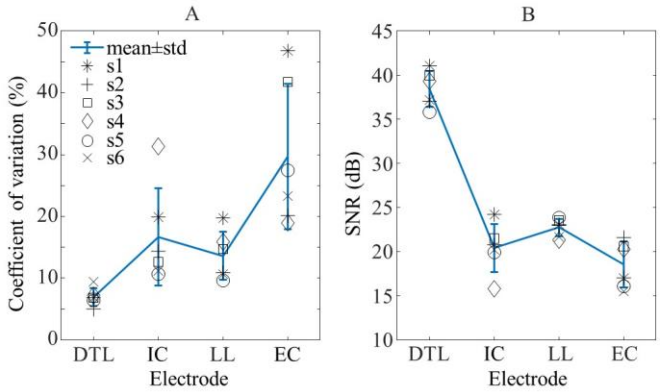

Fig. 2. (A) Coefficients of variation and (B) mean SNR calculated for the a- to b-wave range of each gaze position, for each electrode (DTL, IC, LL and EC) and for each subject (s1 to s6).

(Fig. 1, EC column, red arrows) which show either a positive b-wave ERG morphology (seen in 3/6 subjects) or a very oscillatory signal (3/6 subjects) at the 40° temporal position are gradually replaced by a negative b-wave ERG (seen in 5/6 subjects; no complete inversion was distinguished for the other subject) as we progressively move towards the 40° nasal position.

Compared to the DTL electrode recordings, those obtained with the EC electrode have greater morphological differences, as shown in Fig. 1, which are accompanied by a greater difference in amplitude. Indeed, as shown in Fig. 2A, the DTL electrode has a CV = 7%, which is 23% smaller than the EC electrode's CV value of 30%, it being the largest of all the electrodes. As comparison, the maERG electrode which has the smallest CV is the LL electrode at 14%, which is still twice as large as that of the DTL electrode. To demonstrate that the increase in CV mostly reflects an increase in b-wave amplitudes rather than a change in the baseline noise, the signal to noise ratio (SNR) for each gaze position was calculated and then averaged across gaze positions. The SNR was calculated using Equation 8 below, where the noise variance is the square of the standard deviation of the baseline signal (i.e., first 20 ms of recording before the flash onset). The SNR level is stable (21±5dB) across each skin electrode (Fig. 2B), while the DTL electrode has a 2 times better SNR level (38±3dB). Thus, the change in CV level between skin electrodes is not due to changes in noise level.

Thus, compared to the unchanging ERG waveforms obtained with the DTL electrode, ERG responses recorded with the IC and EC electrodes show positional variations suggesting different ERG derivations and/or dipole orientation changes, features that are essential in order to construct a retinotopic map of sources of retinal activity by solving the inverse problem. Furthermore, this constant DTL signal is consistent with constant illumination of the retina, no matter the gaze position, as a full-field light source is used (with the Ganzfeld).

III. Reconstructions of the Retinal Electrical Activity From the maERG

A. Source Localization on the Retina: From maERG to Retinal Sources

1) The Forward Problem

The first step in the acquisition of a functional retinal map is to compute a generative model of ERG electrodes potential generators. Thus, the linear forward model is given by the following equation:

$$M(t) = GJ(t) + E(t) \quad (1)$$

where M represents the column vector of the measures collected at the (virtual) electrodes, J represents the matrix of the dipolar sources (uniformly distributed over the retina and perpendicular to it) and G is a lead field matrix of the generative model relating each source with each electrode. An additional term E(t) is also added representing the noise in the measurements.

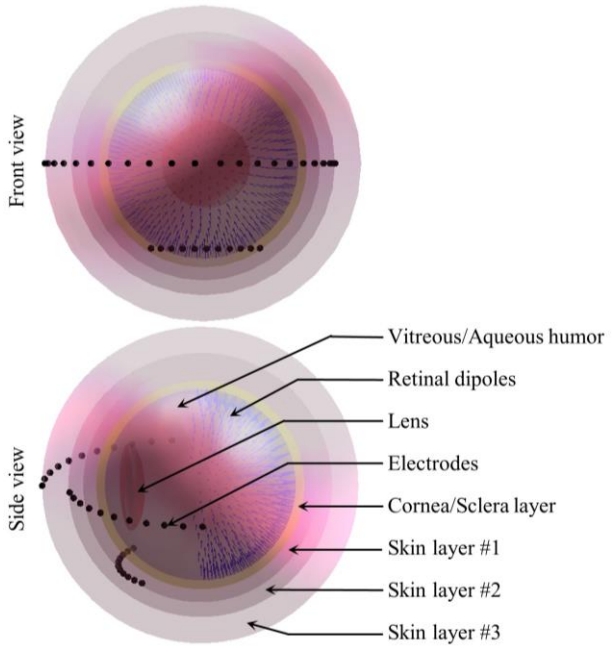

Fig. 3. Front and side views of the BEM eye model used in the study. The dots represent the 33 virtual electrode recording locations on the skin, the blue lines represent the perpendicular dipoles on the retina (spanning 180°), the eye is filed with the vitreous/aqueous humor in grey, the middle red circle represents the lens, the yellow layer represents the corneal/scleral thickness and the 3 outside pinkish layers represent the 3 skin layers.

TABLE I
Radius and Conductivities of Key Tissues in our BEM Model of the Eye.

Tissue	Radius (mm)	Conductivity (S/m)
Combination of Corneal, Scleral and Retinal layers	12	0.41705 (for the cornea)
Vitreous and aqueous humor	11	1.5
Lens	1.04356 anterior, 1.755 posterior and 5 inferior/superior	0.31905
Skin: LL Layer	13.5*	0.0003
Skin: IC Layer	15.2*	0.0003
Skin: EC Layer	18.2*	0.0003
Air	N/A	0

*Value given to model the skin thickness, between each electrode and the eye.

2) The Source Space and Eye Model

In the above forward model, the lead field matrix G is defined from an anatomical model of an emmetropic eye. While small improvements to the model could be made based on each subject's anatomy (obtained for example with MRI or ultrasound), this level of model optimization is outside the scope of this study. As detailed in Table 1, this model is composed of principle layers that are each characterized with respective electrical (conductivities as per [10]) and morphological (radius as per [11] and MNI Brainweb dataset at

http://www.bic.mni.mcgill.ca/brainweb [12]) properties. Of note, the conductivity of the retina used in the model is actually that of the cornea, as its anterior surface has more impact on our model (as per preliminary results). Furthermore, the conductivities of the skin layers represent an average between conductivities of dry and wet skins, as only 1 type of skin layer is present in our model. Since the 3 skin electrodes were not positioned at the same distance of the center of the eye, 3 different layer thicknesses (one per electrode) are modeled.

3) The Generative Model

The forward problem was solved using a Boundary Elements Method (BEM) model [13], as implemented with OpenMEEG [14]. The BEM model was configured with 6 homogenous regions (lens, vitreous and aqueous humor, corneal/scleral and retinal layers, 3 skin layers, air) and 5 borders (external surface of the lens, retina, cornea, 3 skin surfaces), as shown in Fig. 3. Each of these regions is modeled with a regular meshed-sphere of a corresponding radius, except for the asymmetrical lens (see Table 1). We modeled the borders between each ocular region with 1000 uniformly distributed points on a sphere, forming triangular meshes (with the Matlab library developed by Semechko [15]). We decided to model the retina as covering only half of the back of the eye (i.e. 180° of the retina), therefore excluding the area reaching up to the ora serrata. Doing so, we avoid having opposed dipoles in our model (with the region past the 180° point overlapping the region on the back of the eye), as well as limiting the number of privileged dipoles (due to the proximity to the sensors) when calculating the inverse problem. Unfortunately, this also means that a part of the peripheral retina is ignored in our calculations (though given this is a photopic signal, in any case, there are few of these dipoles in this region). Thus, retinal activity is modeled here using only 500 dipoles uniformly distributed over the retina (~1.8mm^2 of spatial resolution per dipole), perpendicular to it and spanning 180° of the back of the eye. However, following a similar reasoning used for the size of the mfERG hexagons, to take into account the non-uniform distribution of the sources on the retinal surface (i.e. cone density decrease from center to periphery), we introduced a diagonal matrix P to weigh the amplitudes of this prior regular distribution of the retinal sources J:

$$M(t) = GPJ(t) + E(t) \quad (2)$$

This correction accounts for the cone density decreasing from the central to peripheral retina (as this study is concentrated on the photopic cone-mediated ERG). The values in the P matrix follow densities per eccentricity reported by Curcio *et al.* [16].

4) The Inverse Problem

Given the maERG measurements and using the previously calculated G matrix (obtained by solving the forward problem with the eye model), we can solve the inverse problem to estimate the sources J. We first multiply the generative model equation in (2) with PG^T:

$$PG^TM(t) = PG^TGPJ(t) + PG^TE(t) \quad (3)$$

By doing so, one can formally inverse the term PG^TGP and isolate the sources:

$$(PG^TGP)^{-1}PG^TM(t) = J(t) + (PG^TGP)^{-1}PG^TE(t) \quad (4)$$

The right-hand-side of this equality exhibits the source J(t) but also a noise contribution. This contribution, present in the data, can be minimized by regularizing the inverse operator in the left-hand side of (4):

$$J^*(t) = (PG^TGP + \lambda W)^{-1}PG^TM(t) \quad (5)$$

The diagonal regularization term λW not only allows to provide a solution despite the presence of noise, but also regularizes the inversion of the ill-posed problem expressed in (4). The solution to this inverse problem is obtained with a value of λ, which represents the best compromise between the goodness of fit (λ=0) and the regularization constraint (J=0 or a large value of λ). To find this compromise (and therefore the value of λ), we simultaneously minimize the goodness of fit (i.e. $\|M(t) - GPJ^*(t)\|$) and the gradient of the solution (i.e. $\|J^*(t)\|^2$) by sampling across different values of λ. To define λW, we have considered two regularization approaches: the Minimum Norm Estimate (MNE) and the Low Resolution Electromagnetic Tomography (LORETA) algorithm.

- The LORETA algorithm consists of defining $W=B^2$, where B represents how the sources are spatially organized, in order to obtain a spatially smooth solution [17]. B is obtained from the adjacency matrix, which describes the neighborhood of each source. This adjacency matrix is then squared and the sum of each row is removed, to obtain an algebraic expression of an estimate of the spatial gradient over the sources. Minimizing the gradient of J(t) amounts to reducing spatial variability (or spatial noise) of the solution.
- The MNE algorithm consists of defining W=I [18].

5) Data Representation of Oscillatory Patterns Using the Discrete Wavelet Transform (DWT)

The ERG is a collection of specific waveforms, each with characteristic timing and frequency ranges. These transient oscillations within the ERG signal, which can be better defined in the time-frequency domain using the DWT, were shown to contain valuable diagnostic information [19, 20]. To better represent this idea, we have added the DWT scalograms to the maERG signals in Fig. 1 (see last column). In this figure, only a small proportion of the time-frequency boxes disclose a high energy content. While noise is uniformly distributed on the entire scalogram, use of the high-density boxes alone can increase the ERG signal's signal to noise ratio (SNR) while the discarded ones mostly contain noise. Based on the above, we have previously identified key descriptors of the photopic ERG signal [19, 20], that were calculated as follows:

$$d(j,k) = \int_{-\infty}^{+\infty} M(t)2^{-j/2}\psi(2^{-j}t - k)dt \quad (6)$$

where the ERG signal M(t) is transformed by a wavelet ψ (here the Haar wavelet), as established by Daubechies [21, 22]. This wavelet is scaled by 2^{-j} and translated by $2^{j}k$, thus producing each time-frequency coefficient d(j,k).

Since the inverse problem in (5) is linear, we can directly localize the descriptor of interest. In this case, we chose to describe the activity of the b-wave (which represents mostly bipolar and Müller cell activities) which can be described by two frequency components in the 20Hz and the 40Hz ranges [19, 20]. We chose to use the "40b descriptor" (i.e. b-wave descriptor in the 40Hz range) since it is the largest DWT coefficient of the ERG [19, 20]. It is this descriptor that will be used as our measurements (i.e. $d_{(M)}(j,k)$),

$$d_{(J^*)}(j,k) = (PG^TGP + \lambda W)^{-1}PG^T d_{(M)}(j,k) \quad (7)$$

The solution provided by this equation ($d_{(J^*)}(j,k)$) would then represent the topographical distribution of the activity associated with this specific transient oscillation. This approach has two major advantages, one technical and one clinical. First, since the wavelet is a bandpass filter, this wavelet selection will result in reducing the noise [23]. Second, this solution allows us to target a specific information about a relevant transient oscillation of the ERG.

B. *Numerical Simulations and Validations*

1) *Simulations*

To simulate a functional retina, a transient oscillatory pattern of ~40Hz was induced on the retina, mimicking the ERG frequency component described above (see suppl. Fig. 1 and 2). This was used to simulate signals recorded from each virtual electrode (i.e. using the forward problem). Three different simulation scenarios were considered: 1- simulated normal activity on the retina, where all sources were equally active (Fig. 4A); 2- simulated central scotoma, where central sources were inactivated (Fig. 4B), and 3- simulated peripheral scotoma, where peripheral sources where inactivated (Fig. 4C). We simulated varying extensions of these scotomas, spanning 5% to 30% of the retinal surface (in 5% increments), in order to determine the smallest scotoma that our technique could theoretically detect. For each case, we simulated a total of 10 scotomas (1 per simulation), each with a differing center positioned in a given 3% region of the retina. Additionally, to assess the impact of noise on our technique, we added varying noise levels to our simulation models, ranging from 0dB to 100dB in increments of 5dB, calculated as:

$$\text{SNR} = 10 * \log\left(\frac{[b\text{-}wave\ amplitude]^2}{noise\ variance}\right) \quad (8)$$

Given a uniform noise on each electrode, we scaled the 33 simulated maERG signals according to the SNR calculated on the largest maERG recording and its associated noise. In order to obtain realistic simulations, we have used maERG noise (with no flash) recorded from 2 normal subjects, following the same procedure as detailed in section 2.2 (see suppl. Fig. 1). The resulting reconstructions from each subject are subsequently put together for the analysis.

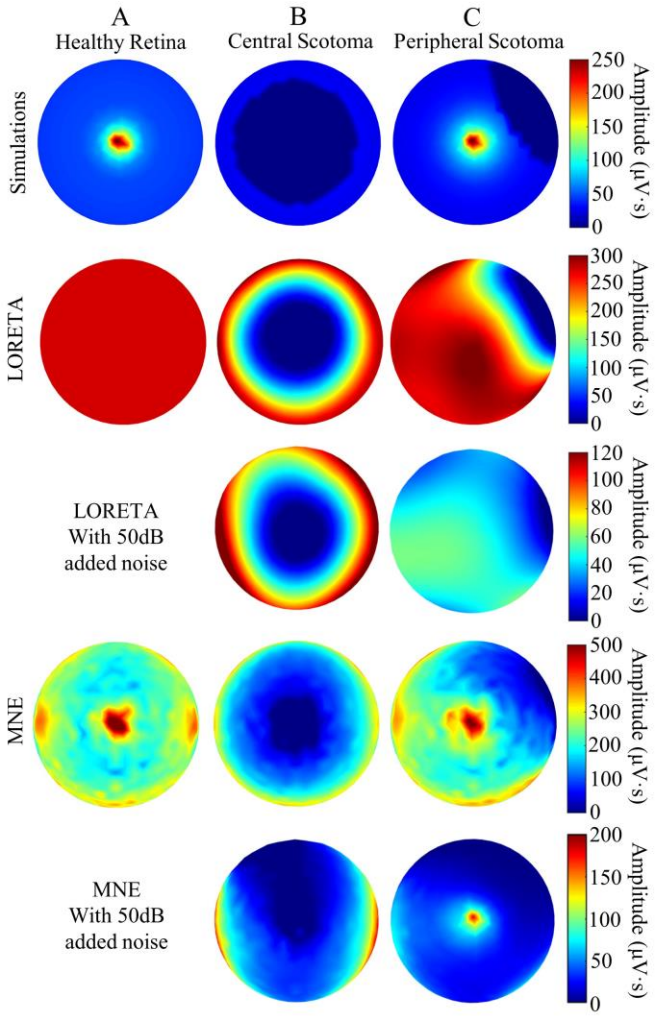

Fig. 4. Simulations (top) with no added noise and their corresponding reconstructions using the LORETA (middle) and MNE (bottom) algorithms. Three types of retinas are modeled: A – a healthy retina, B – a retina with a central scotoma spanning 30% of the retinal surface, and C – a retina with a peripheral scotoma spanning 30% of the retinal surface. An extra row under both types of reconstructions (LORETA and MNE) also show the same reconstruction, though with a 50dB noise level.

2) *Validation of our Method*

To assess the quality of the simulated reconstructions (with varying scotoma sizes and SNR levels), we used the Area Under the Curve (AUC) of the Receiver-Operating Characteristic (ROC) curve obtained by comparing the theoretical (healthy/on state or scotoma/off state) to the reconstructed source distribution (analog value, to which a threshold was applied). By changing the threshold for our reconstructed source distribution, a ROC curve was computed based on fractions of on/off states correctly identified. Sensitivity was the proportion of scotoma states correctly identified. Specificity was the proportion of healthy states correctly identified. A ROC curve with AUC ≥ 0.8 was determined as correctly reconstructing the scotoma. Of note, in our case, the true positive was the (focal) scotoma, which is small compared to the rest of the active retina

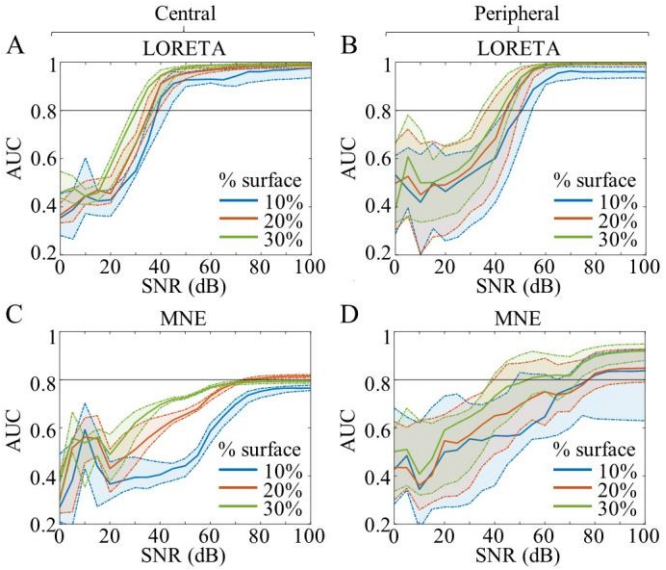

Fig. 5. AUC median (full line) with 25th and 75th percentiles (dotted lines) varying by SNR for different retinal surface ratios, with a threshold of 0.8 (black line). The 1st column (A,C) corresponds to the central inactivity scenarios. The 2nd column (B,D) corresponds to peripheral inactivity scenarios. The 1st row (A,B) corresponds to LORETA reconstructions, while the 2nd row (C,D) corresponds to MNE reconstructions.

(or 'background'). For this reason, the AUC measure was modified following a method proposed for EEG signals [24], by reducing the sampled dipoles of the background (active retina) to equal that of the scotoma. Doing so enables the AUC metric to be balanced with regards to our region of interest and better estimate our algorithm's performance, instead of calculating the AUC of a small area of inactivity on an overwhelmingly active retina (which would imbalance the specificity/sensitivity ratio of the ROC curve).

3) Statistical Analysis

The median, the 25th and the 75th percentiles of the AUC values were calculated for each SNR and scotoma size. Statistical differences between the simulations done were obtained using a 2-way repeated measure ANOVA (with statistical significance at $p<0.05$). Additionally, t-tests were performed to evaluate statistical probability (with $p<0.05$).

IV. Results From the Simulations

A. Image Examples of our 3D Simulated Normal Reconstructions

Representative simulations of retinal dipoles and 3D reconstructions are presented in Fig. 4. The first case shows the simulation of a healthy retina (Fig. 4A). The simulated retinal dipoles have a weighted level of activity based on the cone density distribution, thus explaining why the reconstructions show more activity in the center than in the periphery of the retina. From this simulation of a normal retina, we can derive the ERG recordings predicted at each of the 33 virtual electrodes by solving the forward problem. From these predicted ERG signals, we then solved the inverse problem, either with the LORETA or MNE algorithms, and obtained the reconstructions shown in Fig. 4. As shown, the LORETA algorithm reconstructions reveal a uniform retinal activity map and was unable to reconstruct the foveal singularity (i.e., peak cone density thus peak electrical activity). On the other hand, the MNE algorithm is able to reconstruct the increased foveal activity, as shown by the dark red (i.e. more activity) island of activity at the center of the reconstruction. However, these reconstructions present with a noisier topography (i.e., patchy distribution of active and inactive loci) compared to those obtained with the LORETA algorithm (more compact distribution of active and inactive zones).

TABLE II
Minimal SNR (in dB) Needed With a Median AUC > 0.8

Pathological scenario	Central			Peripheral		
Surface area affected (%)	10	20	30	10	20	30
LORETA	40	40	35	55	45	45
MNE	N/A	75	N/A	80	80	55

N/A means that an AUC level of 0.8 is never reached for this condition.

TABLE III
Minimal Surface Detectable (in %) With a Median AUC > 0.8

Pathological scenario	Central		Peripheral	
SNR (dB)	50	75	50	75
LORETA	10	5	15	5
MNE	N/A	N/A	N/A	25

N/A means that an AUC level of 0.8 is never reached for this condition.

B. Simulated Scotoma Results

Pathological simulations were also attempted, the results of which are shown in Fig. 4 for a central (Fig. 4B) or peripheral (Fig. 4C) scotoma covering 30% of the retina (with no added noise). When using the MNE algorithm, the scotoma limits appear to be either smaller than the real scotoma for central cases (dark blue circle is much smaller in the reconstruction than the simulation), while it appears to be greater than the simulated scotoma for peripheral scotomas, i.e. the suppressed activity (shown in blue) cover a greater area in the reconstruction than in the simulation.

This disparity between ground truth (i.e. the simulations) and the reconstructions is better exemplified with the computed AUC values obtained for each combination of noise level, area of inactivity and scotoma position tested (see Fig. 5). In general, the reconstructions yielded a better fit with the model when using LORETA compared to MNE. An ANOVA comparing the AUC values obtained with the 2 algorithms (LORETA and MNE) yielded a significant difference ($p<0.05$); a difference also seen when comparing the graphs of the first and second rows in Fig. 5 (i.e., comparing Fig. 5A with C, and Fig. 5 B with D); the AUC values obtained using LORETA are always the highest. Furthermore, while the AUC values obtained with LORETA do reach the value of 1 (i.e., perfect reconstruction) with higher SNR, a perfect score is never reached using MNE even with the highest SNRs. Finally, the reconstructions done with the MNE algorithm (Fig. 5C,D) are unable to exceed the 0.8 threshold for central scotoma areas smaller than 30% of the retinal surface, while peripheral scotomas require a high SNR

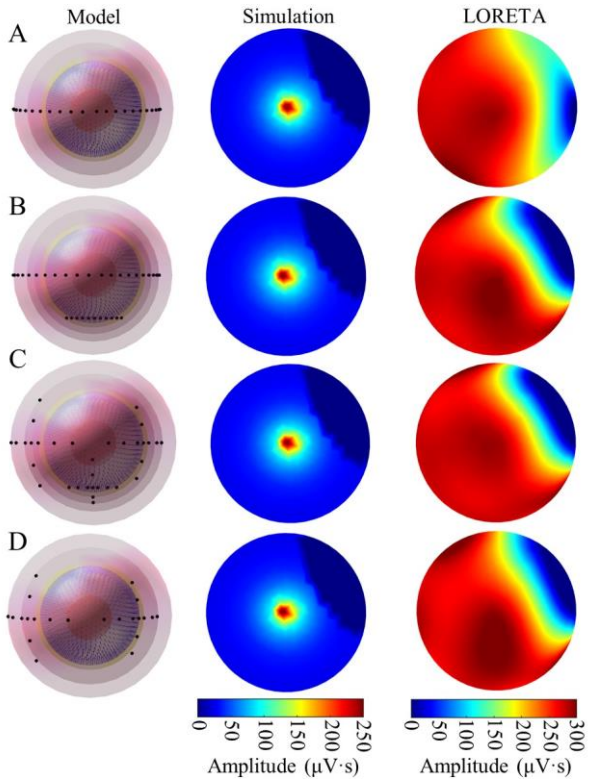

Fig. 6. Retinal activity simulations and its corresponding LORETA reconstructions obtained from 4 different gaze and electrode models. (A) Only the canthus electrodes are present (EC and IC) in this model, with horizontal gazes. (B) The model used in this study: horizontal gazes combined with 3 electrodes (EC, IC and LL). (C) The same 3 electrodes (EC, IC and LL) with 6 horizontal eye movements and 5 vertical eye movements. (D) The same gaze models as in C, though with only 2 electrodes (EC and IC), as in A.

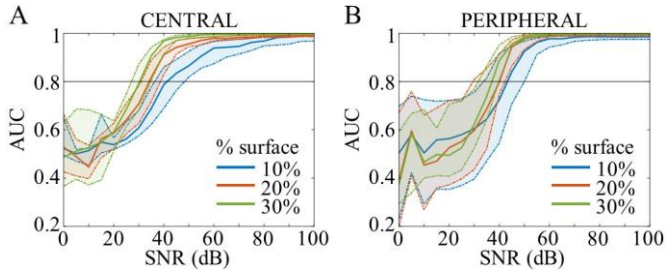

Fig. 7. AUC median (full line) with 25th and 75th percentiles (dotted lines) for the horizontal and vertical gaze movement model (as shown in Fig. 6C) and LORETA reconstructions, varying by SNR for different retinal surface ratios, with a threshold of 0.8 (black line). (A) AUCs for central inactivity scenarios. (B) AUCs for peripheral inactivity scenarios.

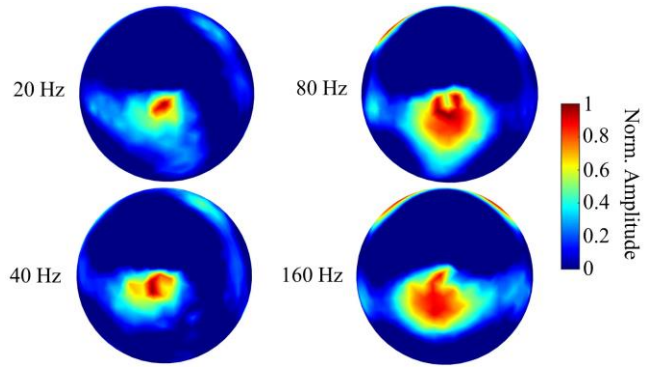

Fig. 8. Retinal activity reconstruction (LORETA) of a normal subject's maERG, from 4 different DWT coefficient bands: 20Hz and 40Hz (a- and b-waves), as well as 80Hz and 160Hz (OPs). The amplitude of each reconstruction is normalized with its maximum to compare each distribution.

(>70dB) to reach this threshold.

When considering the minimal SNR needed to cross the 0.8 AUC threshold, the LORETA algorithm outperformed the MNE algorithm in all cases (see Table 2). The superiority of the LORETA algorithm is also seen when considering the lesion size detectable (i.e., crossing the AUC threshold), as seen in Table 3, where the detection thresholds are smallest with LORETA. Furthermore, Table 2 shows that for reconstructions done with LORETA, the larger the surface of the scotoma is, the lower the SNR level needs to be in order to be detected (with a 5-10dB difference between holes of 10% and 30% of retinal surface).

C. Variations on the maERG recording protocol

To see the effect of the electrode placement, we created a model where the LL electrode was removed, as shown in Fig.6A, thus all electrodes are on the same horizontal plane. The resulting reconstruction has a horizontal bias in the response, where it cannot show the peripheral lesion at its correct location (superior nasal on the retina). Rather, it is placed symmetrically on the horizontal axis of the retina (on the same side as the simulation). On the other hand, putting back the LL electrode enables the correct reconstruction of the simulated retinal activity (Fig. 6B). This result indicates the importance of having virtual electrodes on all 3 planes (i.e. x, y, z coordinates).

Additionally, we tested another experimental strategy to see if including both vertical and horizontal gazes could be of an advantage, as shown in Fig. 6C. The resulting reconstructions show very little differences with the horizontal gaze-only model, a finding also confirmed with the AUC values (Fig. 7; $p<0.05$). Furthermore, if we use a model that combines the EC and IC electrodes with the vertical gaze movements (Fig. 6D), we also have very little differences with the reconstructions where the LL electrode is also used but with only horizontal gazes. This would mean that having an electrode on a different plane (i.e. the LL electrode is lower than the EC and IC electrodes) has the same effect as using vertical gaze movements to change the plane of the virtual electrode. Therefore, the scotomas are correctly localized on the reconstructions as long as there are virtual electrodes on different planes, either because of real electrode placement or gaze angle.

D. Reconstructions from real maERG recordings

Fig. 8 shows reconstructions with LORETA and maERG recordings obtained from a normal subject. As we are now using real ERG signals, we have calculated one reconstruction per each DWT coefficient in the frequency band that describes major components of the ERG, as described by Gauvin et al. [19, 20]. These include a coefficient in 20Hz and one 40Hz

coefficient for the a- and b-waves and two coefficients in the 80Hz and 160Hz for the oscillatory potentials (OPs). All 4 reconstructions show a maximum of activity in the center of the retina, where we expect the peak of macular activity to be located. Of note, each reconstruction varies slightly between each other, with the OP coefficient reconstructions having a broader central activity. The high level of noise in the skin electrode (SNR ≈ 20dB) recording could explain the very low activity in the rest of the retina. Indeed, in those recordings, the noise level was higher than what is shown to be permitted to identify scotomas, though this retina was healthy.

V. Discussion

A. Feasibility of the maERG Recording Technique for Retinal Activity Mapping

In the present study we are proposing a new ERG acquisition technique, termed the multi-angular ERG, that permits the geographic representation of the functional or dysfunctional retina. This new recording and post-processing technique has the advantage of using few real electrodes (only three), thus accommodating both patient comfort and the eye's relatively small size, while at the same time being able to record from multiple virtual electrodes. Indeed, our experiment using a DTL electrode as a control showed that its recordings were not impacted by the changes in gaze position, but the skin electrode (focal electrode) recordings are. This finding indicates that the observed maERG recording variations are indeed multiple ERG derivations and not changes in recording or illumination conditions or trials (i.e. the virtual electrodes can detect changes in retinal dipoles), given the full-field nature of the Ganzfeld. Thus, this justifies the use the maERG recording protocol to carry out the reconstruction of the retinal activity.

The maERG recordings obtained showed some variability between subjects in all electrodes tested, including the DTL. Indeed, for some subjects, the signal did not go through the whole range of modifications (1 subject did not have a b-wave inversion on the EC electrode and half did not lose the b-wave to oscillations on the IC electrode). These differences can be explained by biological differences in the subject's head/eye anatomy which changes the position of the electrodes with respect to the retina (i.e. how much the eye protrudes from the orbit, how the EC electrode is positioned relative to the eye, how large of a shadow the nose creates, etc.). However, this should not considerably affect the quality of the reconstruction, as it relies on the relative amplitude of the signals at each electrode, therefore, it should only modulate the reconstruction's amplitude. If the signal at a given electrode is disproportionately diminished, then this will be seen on the reconstruction as a scotoma, similar to what could happen in a patient. Having a better anatomical landmark than the external canthus would also help reduce this variability. Better yet, placing the electrodes directly on the eye in a manner such that the eye could still rotate relative to the electrode positions would remove this anatomical head variability between subjects as well as increase the signal levels. Of note, the specific impact of fixation errors was beyond the scope of this initial report.

Using this array of ERG signals recorded from different angles, we propose to use an approach originally designed in the context of the electrophysiological signal processing of the brain (EEG) [14] and generalized here in the context of the ERG to reconstruct the retinal activity. The simulated reconstructions of this activity offer intuitive 3D images of the functional retina, enabling a clinician to locate a potential retinal disease.

In order to demonstrate that our technique will yield pertinent diagnostic information when using real world clinical data, we will need to compare the visual fields of patients with clinically demonstrable scotomas (i.e., as per Goldman visual field kinetic perimetry: GVFKP) with the functional retinotopic reconstruction of the focal retinal activity/inactivity obtained with the maERG technique. A perfect match between both scotomas (i.e. evidenced with the GVFKP and with the maERG reconstruction) will validate the diagnostic relevance of our approach. Use of our technique should also allow us to determine if the scotoma experienced by the patient is of retinal (confirmed with abnormal GVFKP and maERG reconstruction) or cortical (confirmed with an abnormal GVFKP but with a normal maERG reconstruction) origin, a conclusion that cannot (in most cases) be reached when the GVFKP data alone is considered.

As for the real maERG reconstructions from a normal subject (Fig. 8), these show an increased activity in the macular region, as expected (though simulated reconstructions of the normal retina in Fig. 4 showed no foveal peak, presumably due to a low energy contrast between center and periphery in our model and the inherent low spatial resolution of LORETA). Interestingly, the 20Hz and 40Hz reconstructions (which are similar and represent the a- and b-wave) differ from those of the 80Hz and 160Hz reconstructions (which are also similar and represent the OPs). This could be explained by the differences in the distribution of the generators for theses specific waveforms, which are either from photoreceptors (a-wave; here cone cells) and bipolar/muller cells (b-wave) [25] and from cells of the inner retina, such as the amacrine cells, and the bipolar cells (OPs) [26-28]. Indeed, the cones are very present in the macula [16], while the horizontal or amacrine cells are running horizontal to it, thus the activity of each cell covers more retinal space, which could in part explain this data. However, this is preliminary data and will have to be better studied in a subsequent publication.

B. Ideal maERG Protocol

According to the AUC metric, results obtained herein show that the reconstructions were most accurate when using the LORETA algorithm, which is focused on the scotoma's accurate reconstruction. However, the images show extreme smoothing of the retinal activity, to the point of not being able to display the expected enhanced activity at the fovea, as the reconstructions from Fig. 4 illustrate. The fact that the fovea cannot be imaged using this approach is probably due to the fact that this method typically favors smooth solutions [17]. This is not the case for reconstructions obtained with the MNE algorithm, which do show the foveal higher activity, while the

reconstructions of the scotomas are noisier and less accurate. However, the MNE algorithm does poorly in the presence of noise, which is seen with the AUC curves but is not imaged here on these noiseless reconstructions. Additionally, our focus is mostly on the correct reconstructions of scotomas, for diagnostic purposes.

We also found that very small scotomas are difficult to detect when the SNR is too low. Indeed, a relatively large SNR is required to obtain adequate results, enabling us to image holes as small as 5% of the retinal surface (with SNR≥75dB needed, see Table 3). Considering the best scenario possible (using the LORETA algorithm), an SNR of 50dB is needed to reconstruct central scotomas (see an example in Fig. 4), while an SNR of 55dB is needed for peripheral ones (for scotomas of 10%). Unfortunately, given that the SNR for skin electrodes is typically low (our recording here had a 21±5dB SNR level), the averaging needs to be high to overcome the poor signal quality (from 21dB to 50dB, a 29dB increase is needed, i.e., 794 times as many flashes), as shown by the noisy maERG signals given in Fig. 1 and an maERG reconstruction in Fig. 8. This brings length to the protocol and increases patient discomfort and fatigue for the test, thus improvements in stimulus, recording, and/or algorithms are needed to make this method more practical. Ideally, and again, to overcome this limitation, the maERG electrodes could be placed directly on the eye, which would greatly improve the SNR level (from 38dB to 50dB, only 16 times more flashes would be needed). This would also remove the need for the skin layers in the model, greatly increase the gaze direction effect on the measurements and thus, simplify the inverse problem-solving algorithm. Alternatively, one could consider using a 30 Hz flicker ERG which would help decrease the testing time, while also gaining functional information. However, in a previous study we showed that the composition of the ERG signal was significantly altered as the rate of stimulation was progressively increased [29]. The latter would suggest that the information thus gathered might yield (functionally) different retinotopic maps.

C. The Advantages of the maERG for Retinal Activity Imaging

Although the idea of using multiple recordings to reconstruct retinal activity by inverse problem solving is not new [6], we believe our novel multi-angular approach provides the best possible solution to the problems of using multiple electrodes close to the eye. Others have proposed alternative solutions, such as placing 8 skin electrodes around the eye [30], though this offered poor reconstructions of the ERG signal (37% difference with the real data when solving the forward problem). More recently, some have considered using a new corneal contact lens electrode array [31] to record multiple ffERG signals simultaneously. The ultimate goal is to use this electrode with their corresponding 3D eye model [32] to solve the inverse problem and map the functioning retina, while they have only solved the forward problem in rats for now. Their electrode array enables them to obtain simultaneous recordings, while ours yields quasi-simultaneous recordings using ‘virtual-electrodes’. However, as theirs is a corneal electrode, a percentage of light is blocked by it, thus forcing them to use stronger illuminations to obtain comparable results. It is also unclear how much of a shadow this electrode produces on the retina, i.e. how much light is unable to reach the retina under each recording electrode location. On the other hand, our present technique using skin electrodes ensures that the light path is unobstructed and undistorted, thus able to reach all areas of the retina. Additionally, our technique also requires no addition of new equipment other than what is currently used in ERG clinics.

Finally, the maERG acquisition technique has the advantage of using a full-field stimulus, unlike the multi-focal ERG (mfERG), which uses a pattern of small hexagonal stimuli to excite small patches of retina, enabling it to detect where an anomaly could lie. Unfortunately, the mfERG stimulus only covers the central 40-50° of the retina [4] and ignores its periphery. Our maERG method reconstructs a functioning retina extending over 180°, thus not only including the central retina but also most of its periphery, albeit not all. Localizing lesion on the whole retina could be particularly useful for diseases originating in the periphery, such as glaucoma [33], a pathology that is characterized by the degeneration of the retinal ganglion cells and the optic nerve.

VI. Conclusion

The maERG acquisition and reconstruction technique presented here can provide a method of reconstructing functional topographical maps of the active retina. This new technique, which makes use of the rotating capability of the eye combined with a limited number of real electrodes, generates multiple ERG recordings (each generated from specific loci on the surface of the retina), as a result of the virtual-electrodes thus created. Solving the inverse problem for these quasi-simultaneous recordings enables us to map the activity produced by the retina in response to a full-field stimulus and gain key topographical information about possible lesions.

References

[1] D. L. McCulloch et al., "ISCEV Standard for full-field clinical electroretinography (2015 update)," Doc Ophthalmol, vol. 130, no. 1, pp. 1-12, Feb 2015.

[2] U. Kretschmann, M. Seeliger, K. Ruether, T. Usui, and E. Zrenner, "Spatial cone activity distribution in diseases of the posterior pole determined by multifocal electroretinography," Vision Res, vol. 38, no. 23, pp. 3817-28, Dec 1998.

[3] E. E. Sutter and D. Tran, "The field topography of ERG components in man--I. The photopic luminance response," Vision Res, vol. 32, no. 3, pp. 433-46, Mar 1992.

[4] D. C. Hood et al., "ISCEV standard for clinical multifocal electroretinography (mfERG) (2011 edition)," Doc Ophthalmol, vol. 124, no. 1, pp. 1-13, Feb 2012.

[5] R. A. Pagon, "Retinitis pigmentosa," Surv Ophthalmol, vol. 33, no. 3, pp. 137-77, Nov-Dec 1988.

[6] K. Davey, B. Thompson, S. Wang, A. Koblasz, and B. Nation, "Predicting distributed retinal source activity from ERG data-Part I: Field theoretic approach," IEEE transactions on biomedical engineering, vol. 35, no. 11, pp. 942-947, 1988.

[7] C. M. Michel and D. Brunet, "EEG Source Imaging: a practical review of the analysis steps," Frontiers in neurology, vol. 10, 2019.

[8] S. Baillet, J. C. Mosher, and R. M. Leahy, "Electromagnetic brain mapping," IEEE Signal processing magazine, vol. 18, no. 6, pp. 14-30, 2001.

[9] M. Hebert, P. Lachapelle, and M. Dumont, "Reproducibility of electroretinograms recorded with DTL electrodes," Doc Ophthalmol, vol. 91, no. 4, pp. 333-42, 1995.
[10] R. Pethig, "Dielectric properties of body tissues," Clin Phys Physiol Meas, vol. 8 Suppl A, pp. 5-12, 1987.
[11] N. Drasdo and C. W. Fowler, "Non-linear projection of the retinal image in a wide-angle schematic eye," Br J Ophthalmol, vol. 58, no. 8, pp. 709-14, Aug 1974.
[12] D. L. Collins et al., "Design and construction of a realistic digital brain phantom," IEEE Trans Med Imaging, vol. 17, no. 3, pp. 463-8, Jun 1998.
[13] J. Kybic, M. Clerc, T. Abboud, O. Faugeras, R. Keriven, and T. Papadopoulo, "A common formalism for the integral formulations of the forward EEG problem," IEEE transactions on medical imaging, vol. 24, no. 1, pp. 12-28, 2005.
[14] A. Gramfort, T. Papadopoulo, E. Olivi, and M. Clerc, "OpenMEEG: opensource software for quasistatic bioelectromagnetics," Biomed Eng Online, vol. 9, p. 45, Sep 6 2010.
[15] A. Semechko. (2019, April). Suite of functions to perform uniform sampling of a sphere. *MathWorks*. [Online]. Version 1.4.0.0.
[16] C. A. Curcio, K. R. Sloan, R. E. Kalina, and A. E. Hendrickson, "Human photoreceptor topography," J Comp Neurol, vol. 292, no. 4, pp. 497-523, Feb 22 1990.
[17] R. D. Pascual-Marqui, C. M. Michel, and D. Lehmann, "Low resolution electromagnetic tomography: a new method for localizing electrical activity in the brain," Int J Psychophysiol, vol. 18, no. 1, pp. 49-65, Oct 1994.
[18] M. S. Hamalainen and R. J. Ilmoniemi, "Interpreting magnetic fields of the brain: minimum norm estimates," Med Biol Eng Comput, vol. 32, no. 1, pp. 35-42, Jan 1994.
[19] M. Gauvin, J. M. Lina, and P. Lachapelle, "Advance in ERG analysis: from peak time and amplitude to frequency, power, and energy," Biomed Res Int, vol. 2014, p. 246096, 2014.
[20] M. Gauvin, J. M. Little, J. M. Lina, and P. Lachapelle, "Functional decomposition of the human ERG based on the discrete wavelet transform," J Vis, vol. 15, no. 16, p. 14, 2015.
[21] I. Daubechies, "Orthonormal bases of compactly supported wavelets," Communications on pure and applied mathematics, vol. 41, no. 7, pp. 909-996, 1988.
[22] I. Daubechies, Ten lectures on wavelets. Siam, 1992.
[23] S. Mallat, "Denoising," in A wavelet tour of signal processing: Elsevier, 1999.
[24] C. Grova, J. Daunizeau, J. M. Lina, C. G. Benar, H. Benali, and J. Gotman, "Evaluation of EEG localization methods using realistic simulations of interictal spikes," Neuroimage, vol. 29, no. 3, pp. 734-53, Feb 1 2006.
[25] L. J. Frishman, "Origins of the electroretinogram," in Principles and practice of clinical electrophysiology of vision: MIT Press, 2006.
[26] L. Wachtmeister. "Oscillatory potentials in the retina: what do they reveal," Prog Retin Eye Res, vol. 17, no. 4, pp. 485-521, 1998.
[27] H. Heynen, L. Wachtmeister, D. van Norren, "Origin of the oscillatory potentials in the primate retina," Vision Res, vol. 25, no. 10, pp. 1365-1373, 1985.
[28] P. Lachapelle, "The oscillatory potentials of the electroretinogram," in Principles and practice of clinical electrophysiology of vision: MIT Press, 2006.
[29] P. Lachapelle, "The effect of a slow flicker on the human photopic oscillatory potentials," Vision Res, vol. 31, no. 11, pp. 1851-57, 1991.
[30] N. Van Schijndel, J. Thijssen, T. Oostendorp, M. Cuypers, and G. Huiskamp, "The inverse problem in electroretinography: a study based on skin potentials and a realistic geometry model," IEEE transactions on biomedical engineering, vol. 44, no. 2, pp. 209-211, 1997.
[31] Y. Krakova et al., "Spatial differences in corneal electroretinogram potentials measured in rat with a contact lens electrode array," Doc Ophthalmol, vol. 129, no. 3, pp. 151-66, Dec 2014.
[32] A. N. Selner, Z. Derafshi, B. E. Kunzer, and J. R. Hetling, "Three-Dimensional Model of Electroretinogram Field Potentials in the Rat Eye," IEEE Trans Biomed Eng, Mar 19 2018.
[33] R. N. Weinreb, T. Aung, and F. A. Medeiros, "The pathophysiology and treatment of glaucoma: a review," JAMA, vol. 311, no. 18, pp. 1901-11, May 14 2014.